



Substrate influence on the vibrational response of gold nanoresonators: Towards tunable acoustic nanosources

R. Delalande , J. Bonhomme , E. Dandeu, L. Becerra, and L. Belliard
Sorbonne Université, CNRS, Institut des NanoSciences de Paris, INSP, F-75005 Paris, France



(Received 15 November 2021; revised 17 December 2021; accepted 11 January 2022; published 20 January 2022)

The development of applications based on metallic nano-objects requires an extensive knowledge of their vibrational properties. Its size, shape, materials, or even crystallinity have a strong influence on the vibrational frequencies of a nano-object. It is also known that the coupling with environment has a strong effect on the lifetime of its resonating modes. However, the impact of the contact between a nano-object and its substrate still requires further investigation. Here we report on the vibrational response of gold disks for different contact area with a silicon substrate. The investigation of the quality factor of the first thickness mode of the disks highlights an important energy transfer from the disks to the substrate. The impact of the size of the contact area on the frequencies of the radial eigenmodes is also reported both experimentally and numerically. Finally, it is shown that such objects can be excited by acoustic waves propagating from the substrate. These findings display the possibility to use nanodisks to develop acoustic microscopy at the nanoscale.

DOI: [10.1103/PhysRevB.105.035422](https://doi.org/10.1103/PhysRevB.105.035422)

I. INTRODUCTION

Metallic nano-objects (mNOs) have received an increasing interest during the past decades due to their high application possibilities. The confinement deeply modifies the properties—optic [1,2], plasmonic [3,4], elastic [5–7]—of a nano-object compared to its bulk counterparts. Therefore, their vibrational properties, which provide information on the thermal or elasticity phenomena at the nanoscale, have been widely studied [8,9]. Several techniques have been proposed to that purpose [10–12]. Developed as a tool to study phonons [13,14], picosecond ultrasonics has quickly been used in order to investigate the vibrational response of mNOs [15–17]. This technique, which allows to measure the vibrations on ensemble [15–17] but also on a single nanoparticle [18–20] have proven to be a very efficient way [21–24]. Therefore, it has been employed in order to study the shape-, size-, or material-dependence of the vibrational response for a large variety of mNOs [15,18,19,25–35]. In particular, it has been shown that the environment greatly affects the vibrations of a mNO, notably the damping rate [34,36–38]. For this reason, prestructured substrates are usually used to study the vibrations of suspended mNOs [23,33,34,39–41]. On the other hand, it has also been highlighted that nano-objects vibrating could be used as sources to generate acoustic waves in the GHz range [20,35,40,42,43]. Such acoustic sources with suboptical sizes are of great interest to perform acoustic imaging. In order to use mNOs as either nanoresonators or acoustic sources, the interaction between these objects and their substrates must be taken into account.

In this paper, we investigated the vibrational response of gold disks with a nanometric thickness for different contact area with their silicon substrate. During the last couple of years, several studies have investigated the vibrations of

similar nanodisks numerically [44–46] and/or experimentally [11,45,47,48]. For example, the crucial role played by the crystallinity of the nanoparticle in the damping process have been highlighted [11,46] and several ways to modulate the frequency or quality factor have been proposed [11,44,47,48]. This paper is complementary to previously published results. A very high diameter-to-thickness ratio implies that both radial and thickness modes can be found in different frequency ranges, allowing to study them independently. Taking advantage of the important diameter, an etching of the silicon substrates allows to investigate partially supported disks. The quality factor of the thickness mode is examined across the radius for different contact area highlighting the energy transfer to the substrate. The generation of acoustic waves in this substrate is shown. The investigation of the radial modes of the disks is also performed and the influence of the etching of the silicon substrate on those modes is examined. Numerical simulations using finite element method (FEM) are performed and a good agreement is obtained between the results obtained experimentally and numerically. Finally, it is shown that acoustic waves propagating from the substrate can be used to excite additional modes of the disk.

II. SAMPLE SYNTHESIS

Using a standard lift-off approach driven by direct laser writing on a positive photosensitive polymer, a network of gold disks with a nominal thickness of $h_D = 100$ nm and a nominal radius of $r_D = 1.7$ μ m spaced out by 20 μ m have been obtained on a SOI(100) wafer. Thereby these disks exhibit a high diameter-on-thickness ratio $\eta = 2r_D/h_D = 34$. A 10-nm chromium layer is added to improve the adhesion of the gold nanostructures. Figure 1(a) introduces an image of this network obtained using a scanning electron microscopy

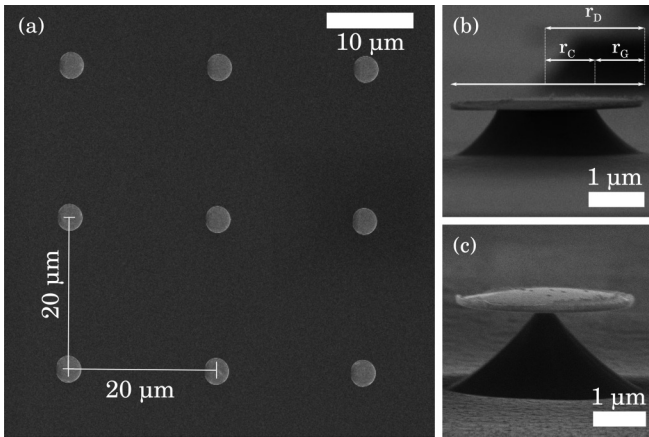


FIG. 1. SEM images of (a) a network of disk, (b) a disk with an etching radius of $r_G = 0.9 \mu\text{m}$, and (c) a disk with an etching radius of $r_G = 1.5 \mu\text{m}$

(SEM). In order to obtain partially suspended disks, the sample can be immersed a couple of seconds in a bath of nitric acid HNO_3 , phosphoric acid H_3PO_4 , and hydrofluoric acid HF . The mixing allows to etch the silicon isotropically and create under the disk a silicon cone supporting partially the latter. The contact surface can easily be modulated by changing the immersion time of the sample in the acid bath. Figures 1(b) and 1(c) show SEM images of two disks with different etching. Partially self suspended disks are therefore characterized by their etching radii r_G as drawn in Fig. 1(b). These images allow to determine the etching radii to be equal to 0.9 and $1.5 \mu\text{m}$ respectively. To be able to study the generation of waves within the substrate, the silicon wafer has also been wet chemically etched using potassium hydroxide KOH in order to obtain a $30\text{-}\mu\text{m}$ thick membrane. An additional layer of 40 nm of aluminum is deposited on the surface of the sample free of disks to optimize the detection and generation processes.

III. EXPERIMENTAL SETUP

Two experimental setups based on a mode-locked Ti:sapphire (MAI-TAI Spectra) laser source operating at 800 nm with a pulse duration below 100 fs at the laser output and a repetition rate of 78.8 MHz have been used. Synchronous detection on the sample reflectivity is performed by modulating the pump beam at 1.8 MHz .

In the first configuration, both pump and probe beams are focused on the sample by means of a microscope objective with a numerical aperture of $NA = 0.95$. This leads to a laser spot size smaller than the disks, of the order of $1 \mu\text{m}$ at $1/e^2$. A two-color experiment is performed by doubling the pump frequency with a nonlinear crystal made of Beta barium borate (or BBO). Therefore, this beam displays a wavelength of 400 nm . The power on the sample of the pump and probe beams are reduced to respectively 1 and 20 mW in order to prevent any damage on the disks. This setup will be referred as the reflection geometry.

In the second setup, both beams are focused on either side of the sample and thereby will be referred as the transmission

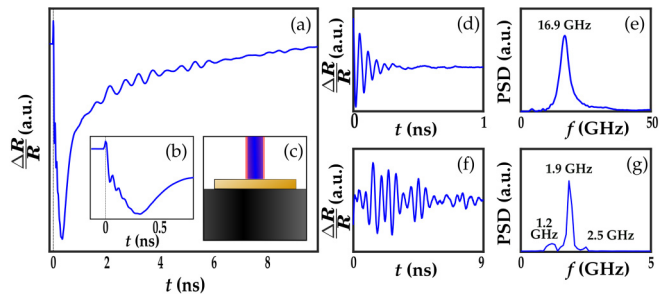


FIG. 2. Variations of reflectivity measured on a gold disk supported on a silicon substrate during (a) 10 ns and (b) 1 ns . (c) Design of the measurement geometry. (d) High frequency oscillations detected just after the excitation and extracted from (a). (e) PSD of the oscillations displayed on (b) and (d) exhibiting a unique component at 16.9 GHz . (f) Low-frequency oscillations detected during several nanoseconds extracted from (a). (g) PSD of these oscillations highlighting 3 components at 1.2 , 1.9 , and 2.5 GHz .

setup. In that case, the pump is focused using an objective with a numerical aperture of $NA = 0.9$ while we use an objective with a numerical aperture of $NA = 0.5$ for the probe beam. The laser spot size of the pump and probe at $1/e^2$ are respectively around 0.5 and $2.0 \mu\text{m}$. The frequency of the pump is not doubled in this case. For both configurations, the sample as well as the objective used to focus the probe beam are installed on top of piezoelectric stages.

A Michelson interferometer allows to detect mainly the normal displacement at the surface.

IV. RESULTS AND DISCUSSIONS

Figure 2(a) exhibits the typical variations of reflectivity $\Delta R/R$ measured when both beams are focused at the center of a fully supported disk using the reflection geometry. A zoom on the first 1 ns of the signal is introduced in Fig. 2(b). The important peak at 0 ps corresponds to the quick change of the optical properties of gold induced by the absorption of the pump photons. This peak indicates the time of arrival of the pump pulse on the sample. It is followed by a slow variation of the transient reflectivity caused by the cooling of gold. Superimposed on this background, two sets of oscillations are also detected. The first one exhibiting high frequency component is measured right after the excitation. A second set with lower frequencies is detected later in the signal.

A. Thickness mode

Power spectrum density (PSD) of the first set of oscillations is shown in Fig. 2(e). Only one component of frequency $f = 16.9 \text{ GHz}$ is identified. These oscillations can be associated to the first eigenmode of the disk along its thickness. Since the acoustic impedance of gold is higher than that of the substrate, we expect a frequency for the thickness mode equal to $c_L/(2h_D)$. Considering a velocity of $c_L = 3.4 \times 10^3 \text{ ms}^{-1}$ in gold, we obtain a frequency of 17 GHz very close to the experimental frequency. The signal exhibited in Fig. 2(d) can be reproduced considering a sinusoidal function decreasing

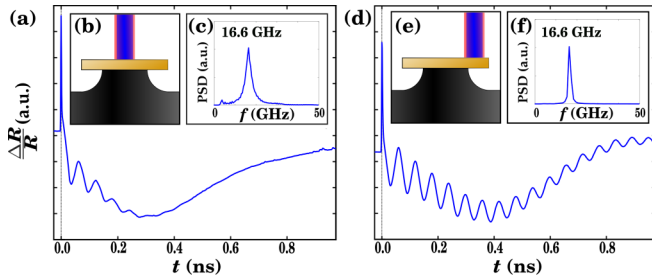


FIG. 3. [(a),(d)] Variations of reflectivity measured respectively on the center and the edge of a gold disk partially supported on a silicon substrate. [(b),(e)] Design of the measurements geometries (c) and (f) PSD of the oscillations extracted from (a) and (d) respectively.

exponentially

$$g(t) = A \cos(2\pi ft + \phi) \exp\left(-\frac{t}{\tau}\right) \quad (1)$$

where A is the amplitude, f the frequency, ϕ the phase, and τ the lifetime of the oscillations. All of these parameters can be extracted from the signal using a minimization algorithm. The quality factor of the oscillations can also be determined as $Q = \pi \tau f$. For the particular case of the signal in Fig. 2(d), we obtain $Q = 5.0 \pm 0.2$. It should be noted here that previous experimental results [44] using objects with lower aspect ratios can result in much higher quality factors (around 100). The authors also demonstrated that if aspect ratio increases the quality factors drop drastically.

The same measurement is realized on both the center and the edge of a disk partially suspended ($r_G = 0.9 \mu\text{m}$). The measured transient reflectivity signals are displayed in Figs. 3(a) and 3(d) respectively and the corresponding PSD are introduced in Figs. 3(c) and 3(f). On the center, the signal obtained is similar to the one in Fig. 2(b) and almost identical values are obtained for the frequency and quality factor of the oscillations : $f = 16.6 \text{ GHz}$ and $Q = 5.1$. The slight difference in frequency can be caused by a small variation of the gold layer thickness during the synthesis process. On the edge of the disk, the same frequency is measured but with a much more important lifetime leading to an increased quality factor $Q = 27.6$.

In order to interpret these results, we remind that the quality factor corresponds to the energy stored over the energy lost in one period. Considering the same excitation, a higher quality factor means fewer losses. Moreover, the quality factor can be decomposed in order to introduce the different channels of relaxation. In our case, the oscillations are decreasing due to intrinsic phenomena as well as radiation towards the environment of the disk. The latter can also be divided in two parts: the air and the silicon substrate contributions. A quality factor can be associated to each process of energy-loose and the global quality factor of the oscillations is thereby decomposed as

$$\frac{1}{Q} = \frac{1}{Q_{\text{int}}} + \frac{1}{Q_{\text{sub}}} + \frac{1}{Q_{\text{air}}}. \quad (2)$$

with Q_{int} , Q_{air} , and Q_{sub} being respectively the contribution from the intrinsic phenomena, the radiation towards the

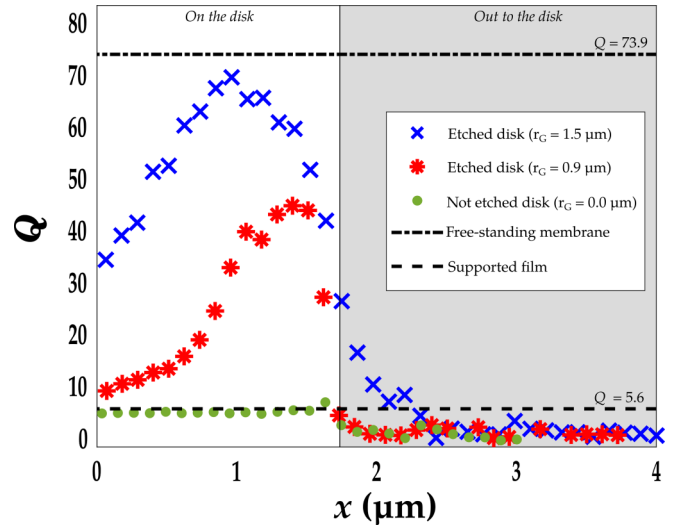


FIG. 4. Values of the quality factor of the first order of the thickness mode obtained experimentally along the radius on three disks displaying different etching times. Values obtained on a self-suspended gold membrane as well as on a film of gold on top of a wafer of silicon are also reported for comparison. Values in the grey area outside the disk are not relevant.

air and the silicon substrate [21,32,34,37,49]. Due to high impedance mismatch between gold and air, radiation is usually neglected implying $1/Q_{\text{air}} = 0$ [21,34].

As shown in the diagrams in Figs. 3(b) and 3(e) the disk is not in contact with the substrate at the edge due to the etching of the silicon. Therefore, the acoustic radiation in the silicon is limited and lead to a higher quality factor at the edge.

In order to investigate the influence of the etching of the substrate on the quality factor of this mode, measurements are performed along the radius of the disks for several etching time. The same frequency is obtained for this mode at different locations. Concerning the quality factor, the obtained results are displayed in Fig. 4. On the sample not etched, the quality factor measured along the radius is nearly constant with a mean value of 4.9 and a standard derivation of 0.2. However, in the case of etched sample, strong variations of the quality factor are exhibited and higher values are obtained closer to the edge than at the center. In the case of $r_G = 1.5 \mu\text{m}$, the contact area becomes smaller than the probe beam size, so the transient signal tends to show an increase of the quality factor due to the suspended areas.

A similar measurement performed on a 100-nm thick self-suspended gold membrane, signifying that $Q = Q_{\text{int}}$, exhibits for the same mode the same frequency and a quality factor of 73.9. This value can be considered as the upper limit of the quality factor associated with the intrinsic phenomenon mixing anharmonic decay and diffusion related to gold crystallites.

A measurement is also realized on 100-nm thick gold film on top of a silicon wafer. The mode is once again detected with a frequency of 16.5 GHz and a quality factor of 5.6 ± 0.1 . The slightly larger value detected on the film may be related to fluctuations in the size of the gold crystallites [11,46]. This value is similar to those obtained on the disk on the substrate.

Using the value of Q_{int} determined on the free-standing membrane and the mean value of Q measured on a fully supported disk, it is possible to determine Q_{sub} from the expression (2)

$$Q_{\text{sub}} = \frac{Q Q_{\text{int}}}{Q_{\text{int}} - Q}. \quad (3)$$

We obtained thereby the value of $Q_{\text{sub}} = 5.2$. This value characterizes the interface between gold and silicon. It can be used to determine experimentally the reflection coefficient for a longitudinal wave with a normal incidence at interface between gold and silicon. Indeed, this coefficient can be simply defined as the ratio of amplitude at two time separated by a period of the oscillations. Considering expression (1), the ratio can be simplified to

$$R = \exp\left(-\frac{\pi}{Q_{\text{sub}}}\right). \quad (4)$$

The obtained value is $R = 0.55$. It is slightly higher to the one calculated using the acoustic impedance Z_c of the two materials

$$R = \left| \frac{Z_{cSi} - Z_{cAu}}{Z_{cSi} + Z_{cAu}} \right|, \quad (5)$$

which is equal to 0.54 when taken the impedance $Z_{cAu} = 65.5 \times 10^6 \text{ kg s}^{-1} \text{ m}^{-2}$ and $Z_{cSi} = 19.5 \times 10^6 \text{ kg s}^{-1} \text{ m}^{-2}$ respectively for the gold and silicon. It means that the interface is not perfect which was anticipated notably because we have a polycrystalline gold. The role played by the thin layer of chromium can be neglected here because its thickness is much smaller than the acoustic wavelength.

Measuring the quality factor at different positions along a disk with an etched silicon substrate can also be used to determine the radius of the contact. Considering that the quality factor can be described by a step function between two values $Q_1 = 5$ or $Q_2 = 74$ corresponding respectively to the part in contact or suspended, the profiles presented in Fig. 4 can be described by the convolution product of this function with a Gaussian profile of the probe. Taking into account a width at half-height of about $0.6 \mu\text{m}$ for the probe beam, we obtain two etching radius equal to $0.85 \mu\text{m}$ and $1.41 \mu\text{m}$. These values are in good agreement with those measured in Figs. 1(b) and 1(c).

B. Acoustic generation

We notice from the measurement realized on the supported membrane that $Q_{\text{sub}} \ll Q_{\text{int}}$. It means that much more energy is lost by acoustic transmission into the silicon substrate than due to the intrinsic phenomena. To investigate the generation within the substrate, we use the second experimental setup in transmission geometry. The pump beam is focused on the surface exhibiting the disks while the probe is focused on the aluminum layer on the other side as drawn in Fig. 5(b). The variation of reflectivity measured when the pump beam is focused on the silicon surface exhibit several echoes due to the acoustic waves propagating within the membrane. In particular, we identify a step due to the longitudinal wave which have crossed the silicon once, Fig. 5(a). When the pump beam is placed on top of a disk, the longitudinal echo exhibit a transient signature shifted in time around 84 ps. The delay leads

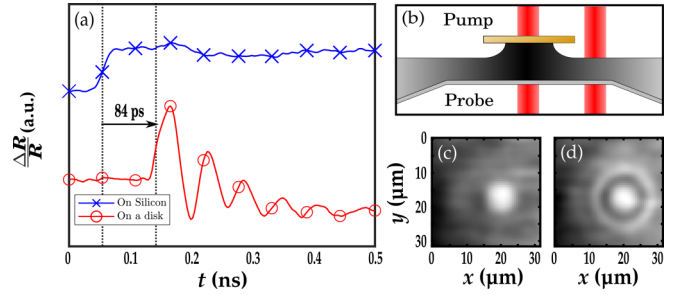


FIG. 5. (a) Variation of reflectivity measured for a pump excitation located on a disk and on the silicon. (b) Design of the measurement geometry. [(c),(d)] Cartography of the variation of reflectivity with separation time equal to 60 ps.

to an estimation of the cone height of $0.71 \mu\text{m}$. The etching of the silicon being isotropic, it implies that $r_G = h_D = 0.71 \mu\text{m}$ and $r_C = 0.99 \mu\text{m}$. Moreover, as shown in Fig. 5(a), oscillations displaying a frequency of 16.8 GHz and a quality factor of 5.2 ± 0.1 are identified. Those oscillations correspond to the waves generated from the disk by the thickness mode at each period. The acoustic snapshots around the epicenter shown in Figs. 5(c) and 5(d) at two different times separated by 60 ps exhibit a quasi-isotropic emission in good agreement with the very low anisotropy of the silicon longitudinal sound velocity around an 4th order symmetry. Those results demonstrate the possibility to use such resonators as acoustic sources at the nanoscale. The frequency of these longitudinal waves being fixed by the thickness and the nature of the disk, it is thus possible to obtain tunable acoustic sources. In the case presented in Fig. 9, the size of the emission zone is about $2.0 \mu\text{m}$. Nevertheless, in a near future it will be possible to study the emission of a source presenting sizes comparable or lower than the emitted wavelength, making possible to modulate the diffraction of the latter. It will also be possible to obtain sizes of sources much smaller than what is usually possible by simple focusing of the excitation which is still limited by optical diffraction.

C. Radial modes

The second set of oscillations extracted from signal 2(a) and after removing the thermal response are shown in Fig. 2(e) and its PSD is represented in Fig. 2(f) exhibiting three components at 1.2, 1.9, and 2.5 GHz. Each of them can be associated to a radial eigenmode displaying a normal displacement detected by the Michelson scheme.

The vibrational response of the disk taking into account the substrate can also be investigated numerically. For that purpose, finite element simulations using the commercial software Comsol Multiphysics are performed. A frequency domain study is realized using the Solid Mechanics module. A 2D axisymmetry geometry is considered in order to reduce the computational cost. The geometry used is displayed in Fig 6(a). A gold disk with a radius of $r_D = 1.7 \mu\text{m}$ and a height of $h_D = 100 \text{ nm}$ is considered. Substrate is simulated by a half-sphere with a radius of $r_D + 0.5\lambda_L$ where λ_L is the wavelength of a longitudinal wave in the silicon. In order to simulate an half-infinite domain for the substrate and get rid

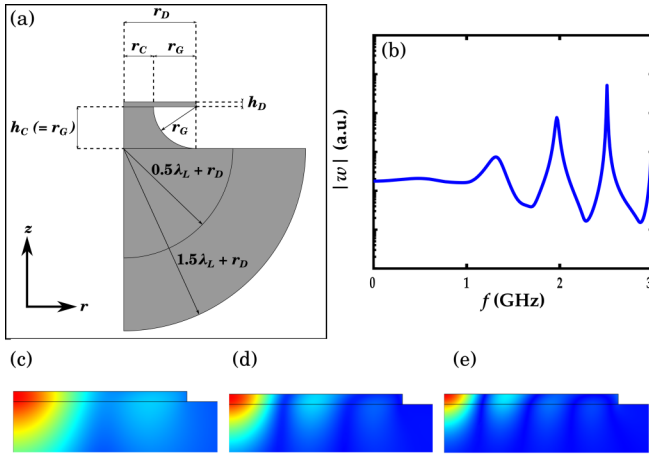


FIG. 6. (a) Drawing of the geometry use during our simulations. (b) Spectrum obtained by a simulation for a disk in contact with silicon substrate. Mode shape of the modes identified at (c) 1.32, (d) 1.98, and (e) 2.52 GHz expressed by the displacement along the z axis.

of the reflections, a second half-sphere is used with a radius of $r_D + 1.5\lambda_L$ and is considered as a perfectly match layer. Both half-spheres are defined as silicon. Properties for both gold and silicon are loaded from the material library provided by Comsol and given in Table I. The maximal size of the element in the gold disk is define as $h_D/5 = 20$ nm and as $\lambda_T/5$ for the silicon parts where λ_T is the wavelength of the transverse wave in silicon which is coherent with [44]. The etching of the silicon is considered by adding a bloc of silicon with a height of r_G and a length of r_D between the disk and the spheres. A sphere of radius r_G centered at the extremity of the disk at the interface between the disk and the bloc is then removed from this bloc. No initial field are applied to the silicon nor the disk. A load defined F_P is applied on the superior frontier on the disk to simulate the excitation by the pump pulse beam. The rest of the frontier are considered free. Spectrum are obtained by integrating the normal component of the displacement field on the superior surface of the disk. This displacement is weighted by F_S simulating the effect of the probe pulse beam. Both pump and probe spatial distribution are simulated by the function

$$F_i(r) = A \exp \left[- \left(\frac{(r - r_0^i)^2}{2(\sigma_r^i)^2} \right) \right] \quad (6)$$

where $i = P, S$ depending if we considered the pump or the probe, $A = 1$ is the amplitude of the function, $r_0 = 0 \mu\text{m}$

TABLE I. Values of the elastic properties used for the finite element simulations.

Material	Young modulus E (GPa)	Poisson ratio ν	Density ρ (10^3 kg/m^3)
Silicon [100]	130	0.28	2.33
Gold	78	0.44	19.3

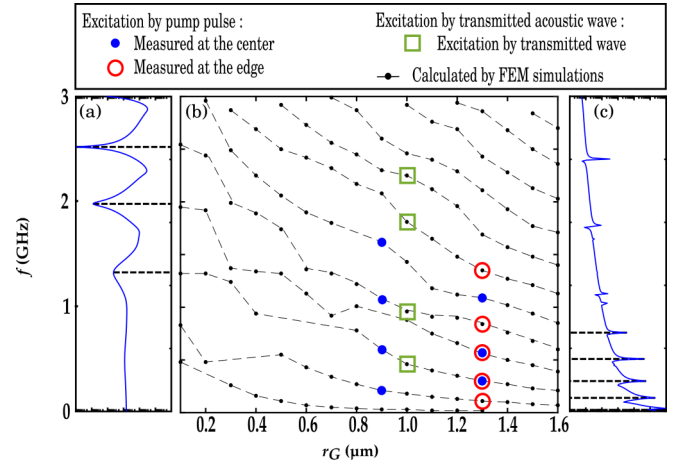


FIG. 7. (a) Spectrum obtained by a simulation for a disk in contact with silicon substrate. (b) Frequency obtained by simulations and identified as modes for different values of r_G . Experimental values are also reported for comparison. (c) Spectrum obtained by a simulation for a free disk without silicon substrate

is the central position of this gaussian function, and $\sigma_R = 0.25 \mu\text{m}$ its width.

The spectrum obtained on a supported disk using those simulations is introduced in Fig. 6(b). It displays three main components at 1.32, 1.98, and 2.52 GHz that are in good agreement with the experimental frequencies observed in Fig. 2(f). The mode shapes of those three modes calculated by finite element simulations are represented in Fig. 6. These shapes displayed a number of nodes and antinodes increasing with the frequency of the modes. Using similar model, the influence of the chromium adhesion layer on the frequency of the modes has been investigated. A slight shift of these frequencies was observed but it remains very weak, of the order of 0.1 GHz or even less, due to the small thickness of this layer compared to the dimensions of the disk.

The results obtained using simulations being coherent with those acquired experimentally, different simulations were performed for several values of the etching radius r_G from 0.1 to $1.6 \mu\text{m}$ with a step of $0.1 \mu\text{m}$. For each value of r_G , mode frequencies are identified and the results are displayed in Fig. 7(b). Frequency of modes with different values of r_G exhibiting similar mode shapes—number of nodes—are identified by a line. The spectra obtained on a disk fully supported and on a free disk are also introduced in Figs. 7(a) and 7(c).

Figure 7(b) highlights that the modes frequencies of the modes decrease as the radius r_G increases. Additionally, the spectra 7(a) and 7(c) clearly show that the quality factor increase as the substrate is removed. The substrate thus leads to an apparent increase in stiffness and as a relaxation channel in the same way as observed on the thickness modes. Figures 8(a) and 8(b) introduce the PSD of the transient reflectivity obtained experimentally at the center of two disks on samples with etching radii of $r_G = 0.9 \mu\text{m}$ and $r_G = 1.3 \mu\text{m}$ respectively. On the first spectrum, a main component is identified at 0.6 GHz in addition to several others components at 0.2, 1.0, and 1.6 GHz. As for the spectrum in Fig. 8(b), the main component is identified at 0.3 GHz in addition to

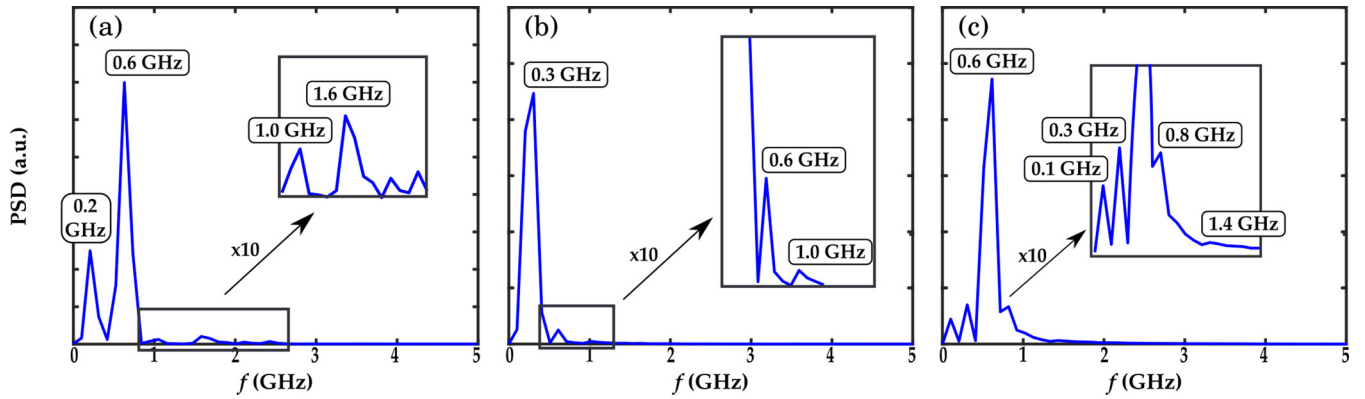


FIG. 8. PSD measured (a) at the center of a disk with $r_G = 0.9 \mu\text{m}$, (b) at the center on a disk with $r_G = 1.3 \mu\text{m}$, and (c) the edge on a disk with $r_G = 1.3 \mu\text{m}$.

two components at 0.6 and 1.0 GHz. FEM simulations gives modes with similar frequencies for those values of r_G . The frequencies determined experimentally are reported in Fig. 7(b) and thereby are associated with frequencies and modes determined numerically. One can notice that the main frequency for both disks can be associated to the same mode, the frequency decrease being due to the increase of the etching radius.

The spectrum in Fig. 8(c) is obtained on the edge instead of the center of a disk with an etching radius of $r_G = 1.3 \mu\text{m}$. It displays different components at 0.1, 0.8, and 1.4 GHz in addition to the components at 0.3 and 0.6 GHz. The comparison between the two spectra in Figs. 8(b) and 8(c) indicates a spatial dependence of the vibrational response measured on the same disk. This spatial dependence is also observed on disks with different etching radius as well as disk without etching. Despite the symmetry breaking induced by an off-axis excitation, no additional modes seem to appear, the experimental frequencies correspond perfectly to the modes with 2D symmetry (see Fig. 7). 3D finite elements simulations, integrating this symmetry breaking, would be likely to confirm this point.

D. Excitation by the substrate

Finally, the possibility to excite a disk through the silicon substrate is investigated. Therefore, the pump beam is focused on the aluminum layer in order to generate waves into the silicon substrate, Figs. 9(b) and 9(c).

Figures 9(a) and 9(d) show the variations of reflectivity $\Delta R/R$ measured when the beams are aligned on the silicon or the disk respectively. On the first one, echoes due to longitudinal waves which have propagated m round trip in the substrate after the initial crossing are identified by L_m . Echoes due to transverse waves are identified similarly by T_m . Several of those echoes are also identified on the spectrum measured on the disk, see Fig. 9(d). Additional oscillations are observed after the echo L_0 . These oscillations as well as the corresponding DSP are displayed in Figs. 10(a) and 10(b) respectively. The spectrum displays two components at 16.3 and 36.6 GHz. Similar oscillations are measured after L_1 . It indicates that the longitudinal waves excites not only the thickness mode of the disk but also its first harmonic. Such oscillations are not found after the peaks corresponding to the transverse waves, proving that the latter does not excite thickness modes. Large

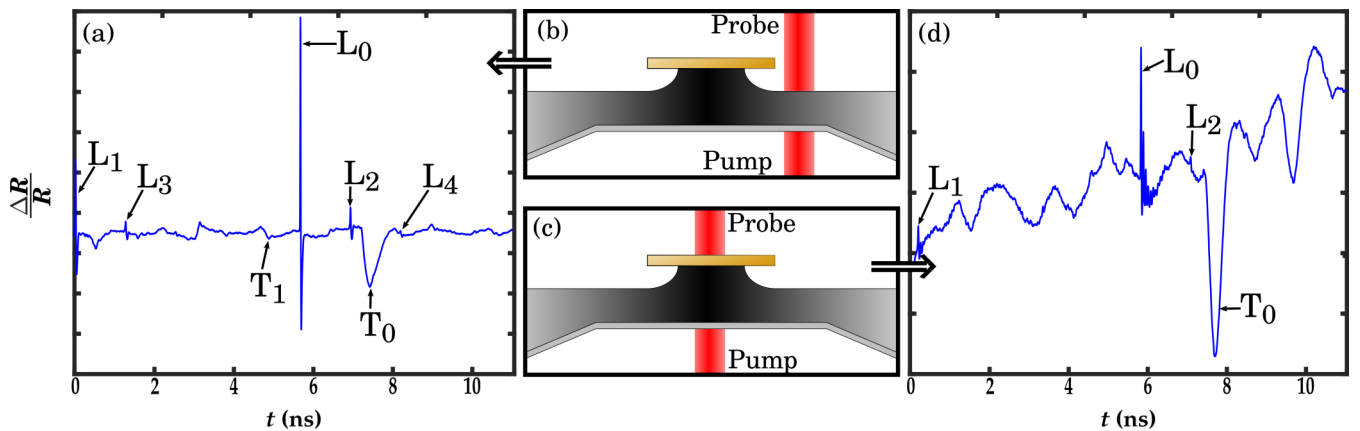


FIG. 9. Variations of transient reflectivity measured on (a) the silicon (d) the gold disk after generation of waves by transmission on the aluminum layer. Design of the measurements geometries on the silicon (b) and the disk (c). The time delay between the L_n echoes give a membrane thickness equal to $28.9 \mu\text{m}$. Using such membrane thickness, the difference in propagation time between longitudinal and transverse waves exhibiting $c_L = 8.4 \times 10^3 \text{ms}^{-1}$ and $c_T = 5.8 \times 10^3 \text{ms}^{-1}$ is estimated at 1542 ps in good agreement with the time delay between L_0 et T_0 measured at 1596 ps.

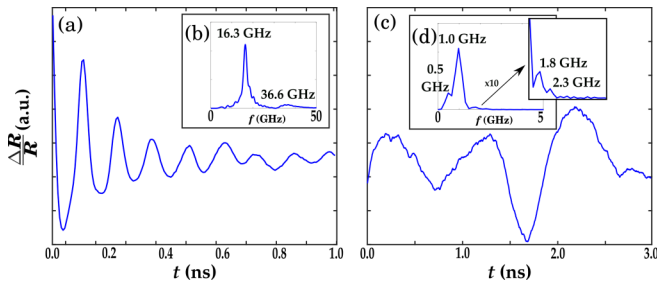


FIG. 10. (a) Oscillations of the transient reflectivity detected after L_0 on signal 9(d). (c) Low-frequency oscillations detected and extracted after T_0 on signal 9(d). [(b),(d)] PSD respectively of signals (a) and (c).

oscillations are also observed in Fig. 9(d), particularly after T_0 as well as T_1 . The spectrum 10(d) of the extracted oscillations 10(c) after T_0 displays a main component at 1.0 GHz and others smaller components at 0.5, 1.8, and 2.3 GHz, each of them corresponding to a radial mode of the disk. However, we were unable to clearly determine if those radial mode are excited by the longitudinal wave, the transverse wave or even both. Due to the additional height of the silicon cone and the thickness of the disk, echoes are measured with a small delay on the disk. Using the delay between the echo L_0 the etching radius, which is equal to the height of the cone, can be determined to be equal to $0.97 \mu\text{m}$. Knowing r_G , the values of the frequency identified are reported in Fig. 7(b). The spectrum obtained by a simulation for $r_G = 1.0 \mu\text{m}$ displays components at similar frequencies : 0.46, 0.96, 1.81, and 2.25 GHz.

It is displayed here that it is possible to excite the eigenmode of such resonator by acoustic waves propagating through its substrate. It must be underlined that some of these modes are located on branches which are not necessarily excited by a direct laser excitation. Indeed, due to the

strong electronic scattering in gold, such excitation generates a volume excitation leading to a different selectivity of excited modes. Therefore, substrate excitation paves the way to a more accurate elastic characterization.

V. CONCLUSIONS

In this study we have investigated the vibrational response of gold disks with a nanometric thickness for different contact area with their silicon substrate using picosecond ultrasonics. Both thickness and radial modes have been identified while measurements are performed directly on the disk. It has been highlighted that the thickness mode loose most of its energy by radiation in the silicon substrate by determining its quality factor on different disks and membranes. We have also demonstrated that the energy radiation in the substrate of this mode generates acoustic wave at the same frequency. This latter depending of the thickness of the disk and of the elastic properties of the material, tunable acoustic wave generation can be achieved by careful design of the disk. We have also demonstrated that the frequencies of the radial modes of the disk are strongly affected by the contact surface area. Indeed, those frequencies decrease importantly when the etching radius increase. These results have been observed experimentally and confirmed using finite element simulations. Finally, we have shown that the eigenmode of the studied disk can be excited thanks to acoustic wave propagation from the substrate. The longitudinal waves were found to excite the thickness mode of the disk as well as its first harmonic. Radial modes have also been excited. The ability to use these disks to generate acoustic waves of nanoscale wavelength associated to the fact that acoustic waves propagating from the substrate can also excite the disks paves the way for the use of these structures to perform nondestructive testing and evaluation and acoustic microscopy at the nanoscale.

-
- [1] E. Lhuillier, S. Keuleyan, and P. Guyot-Sionnest, Optical properties of HgTe colloidal quantum dots, *Nanotechnology* **23**, 175705 (2012).
- [2] N. Moghaddam, C. Grboval, J. Qu, A. Chu, P. Rastogi, C. Livache, A. Khalili, X. Z. Xu, B. Baptiste, S. Klotz *et al.*, The strong confinement regime in HgTe two-dimensional nanoplatelets, *J. Phys. Chem. C* **124**, 23460 (2020).
- [3] P. Yang, J. Zheng, Y. Xu, Q. Zhang, and L. Jiang, Colloidal synthesis and applications of plasmonic metal nanoparticles, *Adv. Mater.* **28**, 10508 (2016).
- [4] L. Wang, M. Hasanzadeh Kafshgari, and M. Meunier, Optical properties and applications of plasmonic-metal nanoparticles, *Adv. Funct. Mater.* **30**, 2005400 (2020).
- [5] M. Rajalakshmi, A. K. Arora, B. S. Bendre, and S. Mahamuni, Optical phonon confinement in zinc oxide nanoparticles, *J. Appl. Phys.* **87**, 2445 (2000).
- [6] G. D. Venkatasubbu, V. Ramakrishnan, V. Sasirekha, S. Ramasamy, and J. Kumar, Influence of particle size on the phonon confinement of TiO_2 nanoparticles, *J. Exp. Nanosci.* **9**, 661 (2014).
- [7] C. E. Bottani, A. Li Bassi, A. Stella, P. Cheyssac, and R. Kofman, Investigation of confined acoustic phonons of tin nanoparticles during melting, *Europhys. Lett.* **56**, 386 (2001).
- [8] L. Saviot and D. B. Murray, Acoustic vibrations of anisotropic nanoparticles, *Phys. Rev. B* **79**, 214101 (2009).
- [9] N. Combe and L. Saviot, Acoustic modes in metallic nanoparticles: Atomistic versus elasticity modeling, *Phys. Rev. B* **80**, 035411 (2009).
- [10] S. Wheaton, R. M. Gelfand, and R. Gordon, Probing the Raman-active acoustic vibrations of nanoparticles with extraordinary spectral resolution, *Nat. Photonics* **9**, 68 (2015).
- [11] C. Yi, M.-N. Su, P. D. Dongare, D. Chakraborty, Y.-Y. Cai, D. M. Marolf, R. N. Kress, B. Ostovar, L. J. Tauzin, F. Wen *et al.*, Polycrystallinity of lithographically fabricated plasmonic nanostructures dominates their acoustic vibrational damping, *Nano Lett.* **18**, 3494 (2018).
- [12] A. Crut, P. Maioli, N. Del Fatti, and F. Valle, Acoustic vibrations of metal nano-objects: Time-domain investigations, *Phys. Rep.* **549**, 1 (2015).

- [13] C. Thomsen, J. Strait, Z. Vardeny, H. J. Maris, J. Tauc, and J. J. Hauser, Coherent Phonon Generation and Detection by Picosecond Light Pulses, *Phys. Rev. Lett.* **53**, 989 (1984).
- [14] C. Thomsen, H. T. Grahn, H. J. Maris, and J. Tauc, Surface generation and detection of phonons by picosecond light pulses, *Phys. Rev. B* **34**, 4129 (1986).
- [15] N. Del Fatti, C. Voisin, F. Chevy, F. Valle, and C. Flytzanis, Coherent acoustic mode oscillation and damping in silver nanoparticles, *J. Chem. Phys.* **110**, 11484 (1999).
- [16] A. Devos, B. Perrin, B. Bonello, and J.-C. Jeannet, Ultra-fast photoacoustics in colloids, *AIP Conf. Proc.* **463**, 445 (1999).
- [17] J. H. Hodak, A. Henglein, and G. V. Hartland, Coherent excitation of acoustic breathing modes in bimetallic core-shell nanoparticles, *J. Phys. Chem. B* **104**, 5053 (2000).
- [18] M. A. van Dijk, M. Lippitz, and M. Orrit, Detection of Acoustic Oscillations of Single Gold Nanospheres by Time-Resolved Interferometry, *Phys. Rev. Lett.* **95**, 267406 (2005).
- [19] P. Zijlstra, A. L. Tchegotareva, J. W. M. Chon, M. Gu, and M. Orrit, Acoustic oscillations and elastic moduli of single gold nanorods, *Nano Lett.* **8**, 3493 (2008).
- [20] A. Amziane, L. Belliard, F. Decremps, and B. Perrin, Ultra-fast acoustic resonance spectroscopy of gold nanostructures: Towards a generation of tunable transverse waves, *Phys. Rev. B* **83**, 014102 (2011).
- [21] T. A. Major, S. S. Lo, K. Yu, and G. V. Hartland, Time-resolved studies of the acoustic vibrational modes of metal and semiconductor nano-objects, *J. Phys. Chem. Lett.* **5**, 866 (2014).
- [22] A. Crut, P. Maioli, N. Del Fatti, and F. Valle, Optical absorption and scattering spectroscopies of single nano-objects, *Chem. Soc. Rev.* **43**, 3921 (2014).
- [23] P.-A. Mante, L. Belliard, and B. Perrin, Acoustic phonons in nanowires probed by ultrafast pump-probe spectroscopy, *Nanophotonics* **7**, 1759 (2018).
- [24] G. Beane, T. Devkota, B. S. Brown, and G. V. Hartland, Ultra-fast measurements of the dynamics of single nanostructures: A review, *Rep. Prog. Phys.* **82**, 016401 (2018).
- [25] G. V. Hartland, Measurements of the material properties of metal nanoparticles by time-resolved spectroscopy, *Phys. Chem. Chem. Phys.* **6**, 5263 (2004).
- [26] V. Juv, A. Crut, P. Maioli, M. Pellarin, M. Broyer, N. Del Fatti, and F. Valle, Probing elasticity at the nanoscale: Terahertz acoustic vibration of small metal nanoparticles, *Nano Lett.* **10**, 1853 (2010).
- [27] X. Zhao, Z. Nie, Y. Feng, W. Zhao, J. Zhang, W. Zhang, P. Maioli, and Z.-H. Loh, Ultrafast acoustic vibrations of AuAg nanoparticles with varying elongated structures, *Phys. Chem. Chem. Phys.* **22**, 22728 (2020).
- [28] T. Stoll, P. Maioli, A. Crut, J. Burgin, P. Langot, M. Pellarin, A. Sanchez-Iglesias, B. Rodriguez-Gonzalez, L. M. Liz-Marzn, N. Del Fatti, and F. Valle, Ultrafast acoustic vibrations of bimetallic nanoparticles, *J. Phys. Chem. C* **119**, 1591 (2015).
- [29] M. Fernanda Cardinal, D. Mongin, A. Crut, P. Maioli, B. Rodriguez-Gonzalez, J. Prez-Juste, L. M. Liz-Marzn, N. Del Fatti, and F. Valle, Acoustic vibrations in bimetallic Au@Pd core-shell nanorods, *J. Phys. Chem. Lett.* **3**, 613 (2012).
- [30] B. Ostovar, M.-N. Su, D. Renard, B. D. Clark, P. D. Dongare, C. Dutta, N. Gross, J. E. Sader, C. F. Landes, W.-S. Chang *et al.*, Acoustic vibrations of Al nanocrystals: Size, shape, and crystallinity revealed by single-particle transient extinction spectroscopy, *J. Phys. Chem. A* **124**, 3924 (2020).
- [31] J. Y. Sun, Z. K. Wang, H. S. Lim, V. L. Zhang, S. C. Ng, M. H. Kuok, W. Zhang, S. Firdoz, and X. M. Lu, Brillouin study of confined eigenvibrations of silver nanocubes, *Solid State Commun.* **152**, 501 (2012).
- [32] R. Marty, A. Arbouet, C. Girard, A. Mlayah, V. Paillard, V. K. Lin, S. L. Teo, and S. Tripathy, Damping of the acoustic vibrations of individual gold nanoparticles, *Nano Lett.* **11**, 3301 (2011).
- [33] R. Delalande, L. Burr, E. Charron, M. Jouini, M. E. Toimil-Molares, and L. Belliard, Vibrational response of Au-Ag alloy and porous Au single nanowires probed by ultrafast pump-probe spectroscopy, *Appl. Phys. Lett.* **115**, 083103 (2019).
- [34] T. A. Major, A. Crut, B. Gao, S. S. Lo, N. Del Fatti, F. Valle, and G. V. Hartland, Damping of the acoustic vibrations of a suspended gold nanowire in air and water environments, *Phys. Chem. Chem. Phys.* **15**, 4169 (2013).
- [35] C. Jean, L. Belliard, T. W. Cornelius, O. Thomas, Y. Pennec, M. Cassinelli, M. E. Toimil-Molares, and B. Perrin, Spatiotemporal imaging of the acoustic field emitted by a single copper nanowire, *Nano Lett.* **16**, 6592 (2016).
- [36] C. Voisin, D. Christofilos, N. Del Fatti, and F. Valle, Environment effect on the acoustic vibration of metal nanoparticles, *Phys. B: Condens. Matter* **316**, 89 (2002).
- [37] T. Devkota, D. Chakraborty, K. Yu, G. Beane, J. E. Sader, and G. V. Hartland, On the measurement of relaxation times of acoustic vibrations in metal nanowires, *Phys. Chem. Chem. Phys.* **20**, 17687 (2018).
- [38] T. Devkota, B. S. Brown, G. Beane, K. Yu, and G. V. Hartland, Making waves: Radiation damping in metallic nanostructures, *J. Chem. Phys.* **151**, 080901 (2019).
- [39] C. Jean, L. Belliard, T. W. Cornelius, O. Thomas, M. E. Toimil-Molares, M. Cassinelli, L. Becerra, and B. Perrin, Direct observation of gigahertz coherent guided acoustic phonons in free-standing single copper nanowires, *J. Phys. Chem. Lett.* **5**, 4100 (2014).
- [40] K. Yu, Y. Yang, J. Wang, G. V. Hartland, and G. P. Wang, Nanoparticle-fluid interactions at ultrahigh acoustic vibration frequencies studied by femtosecond time-resolved microscopy, *ACS Nano* **15**, 1833 (2021).
- [41] S. Fernandez, C. Jean, E. Charron, P. Gentile, M.-I. Richard, O. Thomas, B. Perrin, and L. Belliard, In depth characterization of Ge-Si core-shell nanowires using X-ray coherent diffraction and time resolved pump-probe spectroscopy, *J. Appl. Phys.* **126**, 204304 (2019).
- [42] F. Xu, Y. Guillet, S. Ravaine, and B. Audoin, All-optical in-depth detection of the acoustic wave emitted by a single gold nanorod, *Phys. Rev. B* **97**, 165412 (2018).
- [43] Y. Imade, V. E. Gusev, O. Matsuda, M. Tomoda, P. H. Otsuka, and O. B. Wright, Gigahertz optomechanical photon-phonon transduction between nanostructure lines, *Nano Lett.* **21**, 6261 (2021).
- [44] F. Medeghini, A. Crut, M. Gandolfi, F. Rossella, P. Maioli, F. Valle, F. Banfi, and N. Del Fatti, Controlling the quality factor of a single acoustic nanoresonator by tuning its morphology, *Nano Lett.* **18**, 5159 (2018).
- [45] F. Medeghini, R. Rouxel, A. Crut, P. Maioli, F. Rossella, F. Banfi, F. Valle, and N. Del Fatti, Signatures of small morphological anisotropies in the plasmonic and vibrational responses of individual nano-objects, *J. Phys. Chem. Lett.* **10**, 5372 (2019).

- [46] Y. Gan and Z. Sun, Crystal structure dependence of the breathing vibration of individual gold nanodisks induced by the ultrafast laser, *Appl. Opt.* **58**, 213 (2019).
- [47] W.-S. Chang, F. Wen, D. Chakraborty, M.-N. Su, Y. Zhang, B. Shuang, P. Nordlander, J. E. Sader, N. J. Halas, and S. Link, Tuning the acoustic frequency of a gold nanodisk through its adhesion layer, *Nat. Commun.* **6**, 7022 (2015).
- [48] M.-N. Su, B. Ostovar, N. Gross, J. E. Sader, W.-S. Chang, and S. Link, Acoustic vibrations and energy dissipation mechanisms for lithographically fabricated plasmonic nanostructures revealed by single-particle transient extinction spectroscopy, *J. Phys. Chem. C* **125**, 1621 (2021).
- [49] M. Pelton, Y. Wang, D. Gosztola, and J. E. Sader, Mechanical damping of longitudinal acoustic oscillations of metal nanoparticles in solution, *J. Phys. Chem. C* **115**, 23732 (2011).